Journal of
Composites Science

MDPI

Article

Effect of Modification of Mesoporous Bioactive Glass with Cucurbit[n]urils (n = 6, 7, 8) on the Structural and Physicochemical Characteristics of Composite Biomaterials

Gulstan Zhumabayeva [1,*], Arthur Ukhov [2], Shohreh Mashayekhan [3], Maxim Susid [2], Andrey Khlebnikov [2], Abdigali Bakibaev [2], Irina Kurzina [2], Roza Ryskaliyeva [4] and Rakhmetulla Yerkassov [1]

[1] Department of Chemistry, L.N. Gumilyov Eurasian National University, Astana 010000, Kazakhstan
[2] Faculty of Chemistry, National Research Tomsk State University, Tomsk 634028, Russia
[3] Department of Chemical and Petroleum Engineering, Sharif University of Technology, Tehran 11365-8639, Iran
[4] Department of General and Inorganic Chemistry, Al-Farabi Kazakh National University, Almaty 050000, Kazakhstan
* Correspondence: gulistan.zhumabayeva@gmail.com

Abstract

The surface functionalization of mesoporous bioactive glasses (MBGs) is of critical importance for the development of advanced hybrid biomaterials with controlled interfacial and adsorption properties. Composite systems based on MBGs modified with cucurbit[n]urils (CB[6], CB[7], and CB[8]) were synthesized and systematically investigated to elucidate size-dependent interaction mechanisms and their influence on textural and physicochemical characteristics. Functionalization was achieved via aqueous deposition followed by controlled thermal treatment. Nitrogen sorption analysis revealed distinct pore modification behaviors: CB[6] reduced the specific surface area by 64% with partial pore occupation; CB[7] induced extensive mesopore occlusion (92.4% surface area reduction); whereas CB[8] produced a balanced decrease (71.2%) while largely preserving microporosity. Thermogravimetric analysis demonstrated comparable loading for CB[7] and CB[8], yet MBGs@CB[8] exhibited enhanced thermal stability, with the DTG maximum shifted to ~395 °C. Molecular modeling supported these findings, indicating the lowest adsorption energy for CB[8]. This combination of structural preservation and enhanced stability provides the most favorable balance between pore accessibility and structural modification, demonstrating strong potential as a versatile modifier for subsequent functionalization, including drug loading applications in bone-regenerative systems.

Keywords: mesoporous bioactive glass; cucurbiturils; composite biomaterials; surface modification

Check for updates

Academic Editors: Diego Romano Perinelli and Florentina Lupascu

Received: 31 March 2026
Revised: 30 April 2026
Accepted: 5 May 2026
Published: 8 May 2026

Copyright: © 2026 by the authors. Licensee MDPI, Basel, Switzerland. This article is an open access article distributed under the terms and conditions of the Creative Commons Attribution (CC BY) license.

1. Introduction

Porous inorganic biomaterials have emerged as versatile platforms in regenerative medicine owing to their mechanical integrity and tunable structural architecture [1,2]. Among these, bioactive glasses (BGs) and mesoporous bioactive glasses (MBGs) are distinguished by their ability to undergo surface-mediated reactions that result in the formation of a carbonated hydroxyapatite layer under physiological conditions [3–5]. This bioactivity originates from controlled ion exchange and partial dissolution of the silicate network, leading to the release of biologically relevant species such as Si^{2+}, Ca^{2+} and P^{5+}, which regulate interfacial mineralization processes and stimulate osteogenic

responses [3,4]. Since the seminal discovery of 45S5 Bioglass by Hench in the early 1970s [6,7], bioactive glass chemistry has evolved from composition-driven biocompatibility studies toward the rational design of multifunctional materials with programmable degradation behavior, ion-release kinetics, and surface reactivity [5,8–11].

The development of BGs builds upon the broader evolution of bioceramics in the 20th century. Early generations of ceramic biomaterials, including alumina (Al_2O_3) and zirconia (ZrO_2), were primarily designed for mechanical durability and structural replacement [12,13]. While these materials exhibit excellent wear resistance and mechanical strength, their biological performance is largely bioinert, limiting direct chemical bonding with surrounding tissue. Subsequent advances led to the introduction of calcium phosphate-based ceramics, such as hydroxyapatite and tricalcium phosphate, which display improved biocompatibility and compositional similarity to the mineral phase of bone [14,15]. Nevertheless, these materials typically lack the tunable degradation behavior and dynamic ion-release characteristics required for actively modulating biological responses. In contrast, BGs introduced a fundamentally different concept: a reactive inorganic network capable of controlled dissolution and interfacial reprecipitation processes, thereby enabling chemical integration with biological environments [5,8–11]. This shift from passive structural replacement to chemically interactive biomaterials marked a decisive step toward the design of therapeutic inorganic systems.

The introduction of mesoporosity has been particularly transformative. MBGs synthesized via sol–gel strategies in the presence of structure-directing agents exhibit high specific surface areas, ordered pore architectures, and narrow pore size distributions [5]. These structural features substantially increase drug loading capacity and enable modulation of release kinetics compared to conventional melt-derived glasses. As a result, MBGs have attracted considerable interest as localized drug delivery platforms for bone-regenerative applications [16]. In this context, surface functionalization of porous materials with biologically active compounds, including macrocyclic molecules, has emerged as a promising strategy to enhance loading efficiency and regulate therapeutic release profiles [17–20].

Despite these advances, drug incorporation within MBGs is commonly governed by physisorption and diffusion-controlled release. Conventional systemic drug administration often results in fluctuating plasma concentrations, short therapeutic windows, and potential systemic toxicity [21]. Drug-eluting implants offer a localized and sustained alternative [22–26], yet precise molecular-level control over retention and release profiles remains a significant challenge.

Supramolecular chemistry provides powerful strategies to address this limitation. Macrocyclic host molecules possess well-defined cavities capable of forming stable inclusion complexes through non-covalent interactions [27–29]. Among these systems, cucurbit[n]urils (CB[n]) represent a particularly attractive family of rigid, symmetric macrocycles characterized by carbonyl-lined portals and hydrophobic cavities. Their high binding affinities toward a broad range of guest molecules and exceptional chemical stability make them promising candidates for functionalizing porous inorganic materials [30,31]. CB[n] compounds can selectively encapsulate organic species through host–guest interactions [30,31], and have been widely explored in drug delivery [32,33], diagnostics [34], and therapeutic encapsulation strategies [35–37].

The integration of CB[n] systems with MBGs introduces a hierarchical composite architecture that combines: (i) an osteoconductive inorganic matrix, (ii) a high-surface-area mesoporous network, and (iii) supramolecular host–guest recognition motifs. Such hybrid systems are expected to enhance drug loading via inclusion complex formation, improve molecular retention beyond simple physisorption, and enable release behavior governed by

supramolecular interactions rather than diffusion alone. Although MBGs and cucurbituril host–guest chemistry have been extensively studied independently [32], their direct integration into bioactive glass frameworks and the influence of macrocycle cavity size on interfacial interactions and functional performance remain insufficiently explored.

Although MBGs and the chemistry of cucurbit[n]urils have been intensively studied independently, their direct integration into a single composite system, as well as the systematic influence of the macrocycle cavity size on the nature of interfacial interactions and functional properties, remain insufficiently investigated. In contrast to previous studies, which were primarily focused on the adsorption of CB[n] onto dense substrates (hydroxyapatite, titanium nickelide) [27,28,38], the present study provides, for the first time, a comprehensive comparative analysis of three homologues (CB[6], CB[7], and CB[8]) within a single mesoporous MBG matrix. This approach enables the identification of the optimal system for the subsequent development of biomaterials for various applications.

In this context, we report the fabrication of composite biomaterials based on MBGs functionalized with cucurbit[6], cucurbit[7], and cucurbit[8]urils. By systematically comparing macrocycles of different cavity dimensions, we investigate their impacts on surface chemistry, structural characteristics, and supramolecular interactions within the inorganic framework. Comprehensive physicochemical characterization is employed to elucidate structure–function relationships governing these hybrid systems, providing insight into the rational design of inorganic–supramolecular composites for controlled therapeutic delivery and advanced bone-regenerative applications.

2. Experimental Section

2.1. Synthesis and Isolation of Cucurbit[n]uriles

Cucurbit[n]urils (CB[n], n = 6, 7, 8) were synthesized according to a previously reported procedure with minor modifications [39]. Paraformaldehyde (4.22 g, 0.14 vmol) was dissolved in 10 M sulfuric acid (14 mL) in a three-necked round-bottom flask equipped with a magnetic stirrer and reflux condenser (Figure 1). After complete dissolution, glycoluril (10.0 g, 0.07 mol) was added portionwise under continuous stirring to minimize premature oligomerization. The reaction mixture was heated at 95 °C under reflux for 24 h.

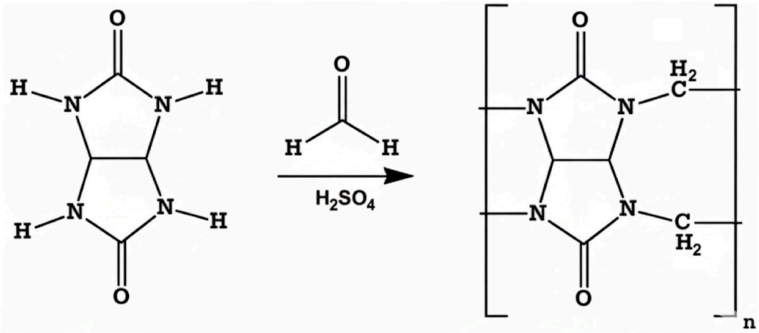


Figure 1. Schematic representation of CB[n] synthesis, where n = 6, 7, 8.

After cooling to room temperature, the reaction mixture was concentrated to dryness. The resulting solid was ground to a fine powder and suspended in distilled water (150–200 mL), followed by stirring at room temperature for 24 h. The suspension was filtered to afford aqueous extract 1. The remaining solid residue was resuspended in distilled water (150–200 mL) and stirred at 40 °C for 24 h. After filtration, aqueous extract 2 and an insoluble residue (Residue 1) were obtained. Aqueous extracts 1 and 2 were combined and concentrated under reduced pressure to a final volume of 10–15 mL to yield a concentrated CB[n] solution.

Isolation of CB[7]. Methanol (80 mL) was added to the concentrated CB[n] solution, and the mixture was stirred at room temperature for 24 h. The precipitated solid was collected by filtration and dried in a vacuum oven at 60 °C for 12 h to obtain CB[7] as a white crystalline powder.

Isolation of CB[8]. The previously obtained insoluble residue (Residue 1) was treated with 40% formic acid (15 mL) under stirring. After dissolution of the acid-soluble fraction, the mixture was filtered. The undissolved solid was collected (Residue 2), while the filtrate was retained for further processing. Residue 2 was recrystallized from concentrated hydrochloric acid to yield crystalline CB[8].

Isolation of CB[6]. The filtrate obtained from the formic acid treatment (vide supra) was evaporated to dryness. The resulting solid was washed with distilled water (20 mL) and subsequently recrystallized from 8 M HCl to produce crystalline CB[6].

The identities and structural integrity of CB[6], CB[7], and CB[8] were confirmed by comparison of their Powder X-Ray Diffraction (PXRD) patterns with reference data from the Cambridge Crystallographic Data Centre (CCDC): CB[6] (CCDC 7209204), CB[7] (CCDC 1428201), and CB[8] (CCDC 883371). The diffraction patterns (Figures S1–S3) were consistent with previously reported data [27,28].

2.2. Synthesis and Surface Functionalization of Mesoporous Bioactive Glass

Mesoporous bioactive glass (MBG) nanoparticles were synthesized via a sol–gel method using tetraethyl orthosilicate (TEOS) as the silica source, calcium nitrate, and triethyl phosphate in an acidic aqueous medium with Pluronic P123 as a structure-directing agent. The mixture was aged at 40 °C for 48 h, dried, and calcined at 600 °C for 5 h to remove the template and obtain the final porous structure.

Preparation of MBGs@CB[6]. CB[6] (50 mg) was dissolved in distilled water (75 mL) containing 3 M HCl (15 mL) under vigorous stirring. MBGs (50 mg) were added to the solution, and the suspension was stirred at 60 °C for 3 h. The temperature was subsequently increased to 80 °C and maintained for 5 h to promote partial solvent evaporation and the removal of water and hydrochloric acid. When the total volume was reduced to approximately 10 mL, the suspension was transferred to a Petri dish and dried under vacuum (100 mbar) at 60 °C for 24 h to constant weight, affording the composite material MBGs@CB[6].

Preparation of MBGs@CB[7]. CB[7] (50 mg) was dissolved in distilled water (25 mL) under vigorous stirring at room temperature. MBGs (50 mg) were added to the solution, and the mixture was stirred at 60 °C for 3 h. The temperature was then increased to 80 °C and maintained for 2 h to partially evaporate the solvent to a final volume of approximately 10 mL. The resulting suspension was transferred to a Petri dish and dried under vacuum at 60 °C overnight to constant weight, yielding MBGs@CB[7].

Preparation of MBGs@CB[8]. CB[8] (50 mg) was dissolved in deionized water (350 mL) at 60 °C under stirring for 1.5 h. MBGs (50 mg) were subsequently added, and the mixture was stirred at 60 °C for 3 h. The temperature was increased to 85 °C and maintained for 12 h to reduce the solvent volume to approximately 10 mL. The concentrated suspension was transferred to a Petri dish and dried under vacuum at 60 °C for 24 h to constant weight, affording MBGs@CB[8].

2.3. Characterization Methods

Fourier transform infrared (FTIR) spectra were recorded using a Nicolet 6700 spectrometer (Thermo Fisher Scientific, Waltham, MA, USA) equipped with an attenuated total reflectance (ATR) accessory. Spectra were collected in the range 400–4000 cm^{-1} with a

spectral resolution of 4 cm^{-1} and 32 accumulated scans. Reflectance data were converted to absorbance using the Kubelka–Munk transformation.

Morphological analysis was performed using a QUANTA 200 3D scanning electron microscope (SEM) (FEI, Hillsboro, OR, USA) operated in environmental or reduced vacuum mode. Images were acquired at accelerating voltages between 5 and 30 kV, depending on the sample and imaging requirements. Prior to analysis, samples were mounted on aluminum stubs and sputter-coated with a thin conductive layer when necessary.

Powder X-ray diffraction (PXRD) patterns of crystalline CB[6], CB[7], and CB[8] were recorded using an XRD-7000 diffractometer (Shimadzu, Kyoto, Japan) equipped with a Cu Kα radiation source (λ = 1.5406 Å). Data were collected in the 2θ range of 5–50° at a scan rate of 30° min^{-1}. Phase identification was performed by comparison with reference data from the CCDC.

Thermogravimetric analysis (TGA) was carried out using an STA 449 F1 Jupiter instrument (NETZSCH, Selb, Germany). Approximately 5 mg of sample was placed in an alumina crucible and heated from 25 °C to 600 °C at a rate of 10 °C min^{-1}. Measurements were conducted under a controlled gas flow (air or argon, 80 and 20 mL min^{-1}, respectively).

2.4. Nitrogen Adsorption–Desorption Analysis

Textural properties, including specific surface area and pore size distribution, were determined by low-temperature nitrogen adsorption–desorption measurements at −196 °C using a 3Flex surface characterization analyzer (Micromeritics, Norcross, GA, USA). Prior to analysis, approximately 100 mg of each sample was degassed under vacuum at 100 °C for 2 h until constant weight was achieved.

The specific surface area (S-BET) was calculated using the Brunauer–Emmett–Teller (BET) method by linear fitting of the adsorption isotherm in the relative pressure (P/P_0) range of 0.05–0.30. The pore size distribution was determined from the adsorption branch using the Barrett–Joyner–Halenda (BJH) model. The total pore volume was estimated from the amount of nitrogen adsorbed at a relative pressure of $P/P_0 \approx 0.995$.

2.5. Molecular Mechanics Calculation of CB[n]-SiO_2 Surface Interactions

Molecular mechanics calculations were performed using HyperChem 7.5 (Hypercube Inc., Gainesville, FL, USA) employing the MM+ force field. The SiO_2 surface was modeled using an α-quartz crystal structure constructed from a 3 × 3 × 3 supercell derived from crystallographic unit cell parameters. Periodicity was not applied; the model represented a finite slab. Prior to adsorption simulations, the geometries of CB[6], CB[7], and CB[8] were fully optimized using the MM+ force field until the root-mean-square (RMS) gradient convergence criterion reached 0.01 kcal mol^{-1} $Å^{-1}$.

Interaction energies between CB[n] and the SiO_2 surface were calculated under the following assumptions: (i) adsorption of cucurbit[n]uril does not induce structural changes in the SiO_2 surface (rigid surface approximation); (ii) no intermolecular interactions occur between adjacent CB[n] molecules (single-molecule adsorption model); and (iii) solvent effects are neglected (gas-phase approximation).

The interaction energy was determined using Equation (1):

$$E_{\text{interaction}} = E_{\text{adsorption}} - E_{\text{deformation}} \quad (1)$$

where $E_{\text{adsorption}}$ is the total energy of the CB[n]-SiO_2 adsorption complex, $E_{\text{deformation}}$ represents the strain energy of the CB[n] molecule upon adsorption.

The deformation energy was calculated as:

$$E_{\text{deformation}} = E_{\text{adsorbedCB[n]}} - E_{\text{optimizedCB[n]}} \quad (2)$$

where $E_{\text{adsorbedCB[n]}}$ is the energy of the CB[n] molecule in the adsorbed geometry, $E_{\text{optimizedCB[n]}}$ denotes the energy of the fully optimized isolated CB[n] molecule. All reported energies are given in kcal mol^{-1}.

3. Results and Discussion

3.1. Rationale for CB[n] Deposition Strategy

Previous studies have demonstrated that the deposition behavior of cucurbit[n]urils (CB[n], n = 6–8) on porous inorganic substrates strongly depends on their solubility and supramolecular association in aqueous media. In particular, deposition on hydroxyapatite revealed that CB[6] and CB[8] tend to form surface aggregates, whereas the higher water solubility of CB[7] facilitates its penetration into the porous scaffold [28]. Subsequent investigations showed that controlled heating of aqueous CB[6] solutions promotes the formation of water-associated supramolecular aggregates, enabling uniform surface coverage of hydroxyapatite and titanium nickelide substrates [17,27].

These findings indicate that aqueous-phase deposition combined with gradual solvent evaporation provides an effective route for achieving controlled surface modification of porous inorganic materials without the use of organic solvents. Such an approach is particularly attractive for biomaterial applications, as it minimizes potential alterations of surface bioactivity and avoids solvent-induced structural changes.

Considering the established bioactivity and ion-release properties of bioactive glasses and MBGs [3–5,23,24], we adopted a similar aqueous deposition strategy for MBG modification. CB[n] was introduced from aqueous solution followed by controlled thermal evaporation at elevated temperature to promote adsorption and surface organization within the mesoporous framework (see Section 2.2).

3.2. FTIR Analysis of MBGs@CB[n] Composites

The successful incorporation of cucurbit[n]urils into the MBG framework was evaluated by FTIR spectroscopy (Figure 2). The spectrum of pristine MBGs is characterized by broad Si–O–Si asymmetric stretching vibrations in the 1040–1100 cm^{-1} region, accompanied by symmetric stretching and bending modes near 800 cm^{-1} and 460 cm^{-1}, respectively. These bands remain present in all modified samples, confirming preservation of the silicate network after surface functionalization.

In the FTIR spectrum of MBGs@CB[6] (Figure 2a), additional absorption bands characteristic of CB[6] are clearly observed. A prominent band at 1726 cm^{-1} is assigned to the stretching vibration of the carbonyl (C=O) groups located at the glycoluril portals. Furthermore, bands in the 1200–1500 cm^{-1} region correspond to methylene ($-CH_2-$) bending vibrations of the macrocyclic framework. Compared to pure CB[6], a slight red shift (~2 cm^{-1}) of the carbonyl band is observed upon adsorption onto MBGs, accompanied by a decrease in CH_2 band intensity. The small red shift suggests the involvement of portal carbonyl groups in weak hydrogen bonding interactions with surface silanol (Si–OH) groups of the BG.

For MBGs@CB[7] (Figure 2b), similar vibrational features are detected; however, the carbonyl stretching band appears at 1694 cm^{-1}. Relative to pure CB[7], a pronounced blue shift of approximately 34 cm^{-1} is observed. The substantial blue shift observed for CB[7] (~34 cm^{-1}) suggests a significant perturbation of the carbonyl group environment, which may indicate stronger hydrogen bonding or coordination-type interactions with surface

silanol groups. However, alternative contributions from changes in molecular packing, local polarity, or confinement effects within the mesopores cannot be excluded. Therefore, the FTIR data should be interpreted as complementary evidence alongside the BET, TGA, and molecular modeling results, rather than as definitive proof of interaction strength. The magnitude of this shift implies that CB[7] exhibits the strongest interaction with the MBG surface among the three homologues.

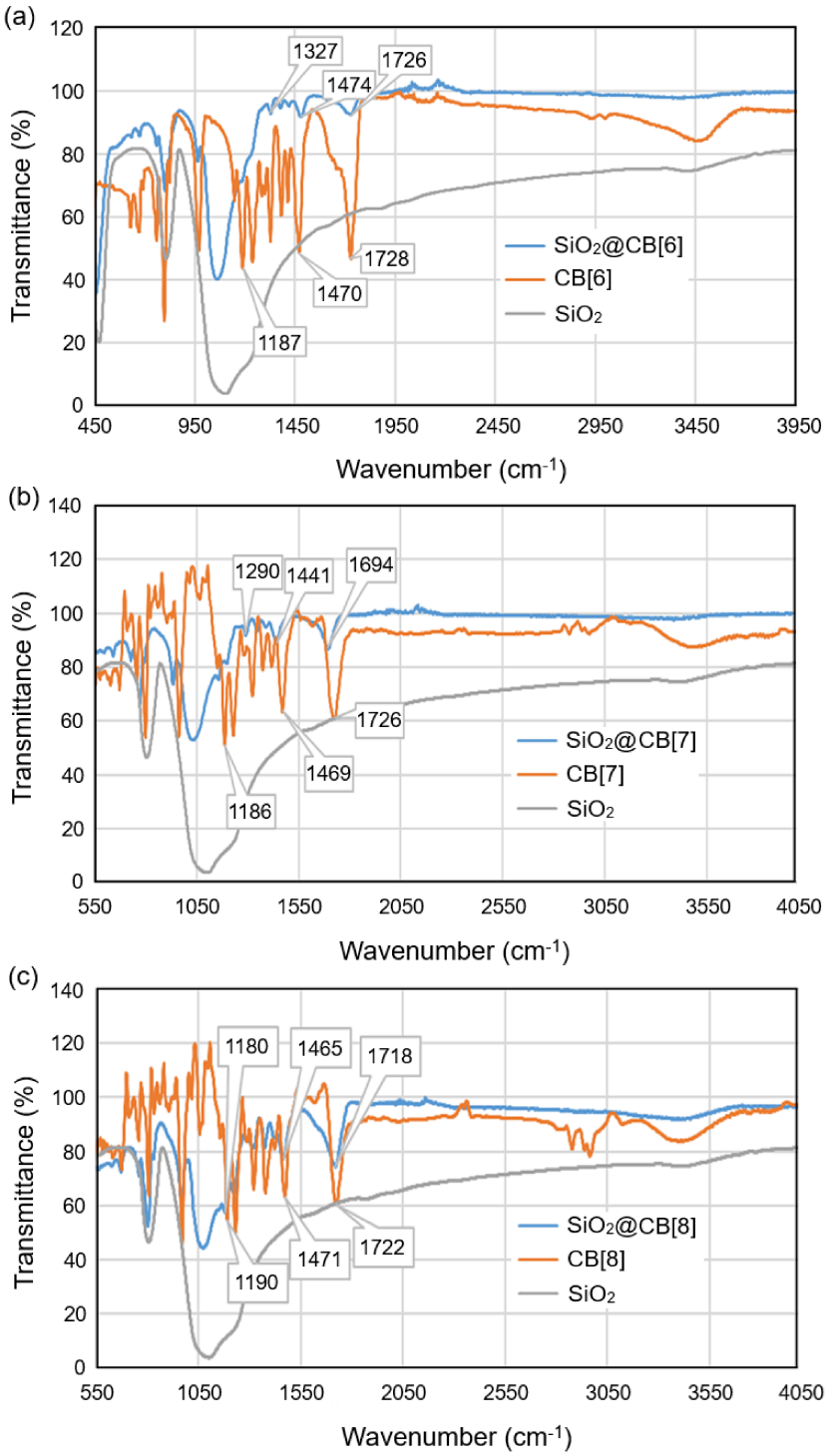


Figure 2. Comparative FTIR spectra of (**a**) CB[6], (**b**) CB[7], and (**c**) CB[8] (orange lines), pristine MBGs (gray lines), and the corresponding MBGs@CB[n] (blue lines) composites. Characteristic stretching vibrations of the cucurbit[n]urils and Si–O–Si framework bands of the mesoporous bioactive glass are highlighted.

Figure 2c also shows characteristic carbonyl and methylene vibrations of the macrocycle for the FTIR spectrum of MBGs@CB[8]. The C=O stretching band appears at 1726 cm^{-1}, with a modest blue shift of approximately 4 cm^{-1} compared to pure CB[8]. This smaller shift indicates weaker or less specific interfacial interactions relative to CB[7], which may arise from steric limitations associated with the larger cavity size of CB[8], restricting optimal surface contact within the mesoporous channels.

A comparative analysis of the carbonyl band shifts reveals a size-dependent and non-linear interaction trend: CB[6] exhibits a slight red shift (~2 cm^{-1}), CB[7] shows a pronounced blue shift (~34 cm^{-1}), whereas CB[8] displays a moderate blue shift (~4 cm^{-1}). The magnitude and direction of these shifts reflect differences in the electronic environment of the portal carbonyl groups upon adsorption. The substantial blue shift observed for CB[7] suggests a significant perturbation of the C=O bond, indicative of stronger interfacial interactions with surface silanol groups of the MBG. This behavior implies that CB[7] achieves the most favorable geometric and electronic compatibility with the MBG surface, potentially enabling more effective alignment and interaction within the mesoporous framework compared to CB[6] and CB[8].

3.3. Surface Morphology Analysis

The surface morphology of pristine MBGs and the corresponding MBGs@CB[n] composites was examined in detail using SEM. As shown in Figure S4, the pristine MBGs sample consists of irregularly shaped conglomerates with dimensions of approximately 20–50 μm. These larger aggregates are composed of densely packed nanoscale primary particles, typical of sol–gel-derived mesoporous bioactive glasses. The observed morphology reflects partial aggregation during drying and calcination processes.

Upon modification with CB[6], the overall conglomerate morphology of MBGs is preserved; however, the surface becomes decorated with smaller particles in the range of 570–900 nm (Figure 3a,b). These nanoscale domains are distributed across the MBG aggregates, suggesting deposition of CB[6] on the external surface and possibly within accessible mesopores. The relatively uniform distribution indicates effective adsorption of the macrocycle under the applied deposition conditions.

In the case of MBGs@CB[7], conglomerates are again observed; however, finely dispersed particles ranging from 700 nm to 3 μm are more clearly distinguishable on the aggregate surfaces as depicted in Figure 3c,d. Compared to MBGs@CB[6], the particles in MBGs@CB[7] appear less prone to secondary aggregation, and interparticle boundaries are more clearly defined. This behavior may be attributed to differences in solubility and interaction strength of CB[7], which could promote more homogeneous surface coverage and reduced interparticle cohesion.

SEM images of MBGs@CB[8] display a similar overall morphology (Figure 3e,f). Large MBG conglomerates are present, decorated with dispersed particles in the range of 600 nm to 2 μm. The distribution appears somewhat less uniform compared to MBGs@CB[7], which may reflect steric effects associated with the larger cavity size of CB[8] influencing its deposition and surface organization.

Importantly, no evidence of structural collapse or significant morphological degradation of the MBG framework is observed after modification with any of the cucurbit[n]urils. The preservation of aggregate morphology indicates that the aqueous deposition and thermal evaporation procedure does not adversely affect the structural integrity of the MBG.

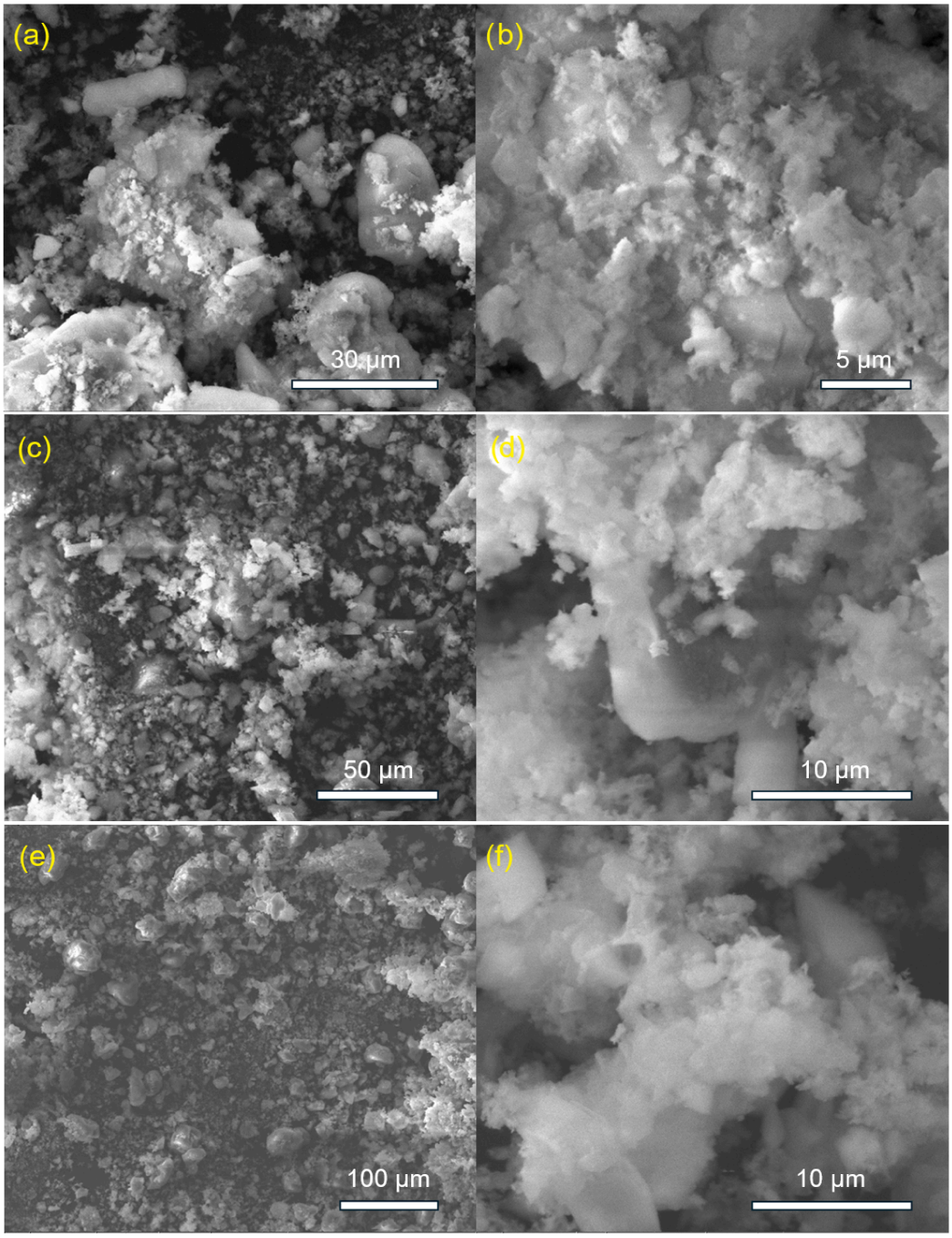


Figure 3. SEM images of MBGs@CB[n] composites at different magnifications: MBGs@CB[6] at 3052× (**a**) and 11,000× (**b**); MBGs@CB[7] at 600× (**c**) and 10,000× (**d**); and MBGs@CB[8] at 600× (**e**) and 10,000× (**f**). The images illustrate the aggregate morphology of mesoporous bioactive glass and the surface distribution of CB[n]-modified particles.

3.4. Textural Properties and Porosity Analysis

The textural parameters of pristine MBGs and the corresponding MBGs@CB[n] composites, including specific surface area, micropore and mesopore surface areas, and pore volumes, are summarized in Table 1.

Pristine MBGs exhibit a specific surface area of 111.66 m^2 g^{-1}, reflecting the presence of a developed mesoporous network. Upon functionalization with cucurbit[n]urils, a substantial reduction in textural parameters is observed, confirming successful incorporation of macrocycles within the porous framework.

Table 1. Comparative textural characteristics of pristine MBGs and MBGs modified with CB[6], CB[7], and CB[8], including specific surface area (BET), micropore and mesopore surface areas, and pore volumes.

Sample	BET Surface Area, $m^2\ g^{-1}$	Micropore Area, $m^2\ g^{-1}$	Micropore Area (BJH Adsorption), $m^2\ g^{-1}$	Micropore Volume, $cm^3\ g^{-1}$	Total Pore Volume, $cm^3\ g^{-1}$
MBGs	111.66	16.75	92.8	0.0061	0.42
MBGs@CB[6]	40.25	7.95	33.3	0.0029	0.20
MBGs@CB[7]	8.48	12.99	3.9	0.0047	0.03
MBGs@CB[8]	32.13	14.49	18.2	0.0059	0.13

Modification with CB[6] results in a 64% reduction in specific surface area relative to pristine MBGs. The micropore and mesopore surface areas decrease by 52.5% and 64.1%, respectively, accompanied by reductions in micropore and mesopore volumes of 52.5% and 52.4%. These results indicate partial occupation of both micro- and mesopores. The relatively uniform decrease across pore types suggests that CB[6], due to its compact size, can access and distribute within the porous network without completely blocking the mesostructure.

In contrast, MBGs@CB[7] exhibits a dramatic reduction in specific surface area to 8.48 $m^2\ g^{-1}$ (92.4% decrease), representing the most pronounced textural change among the studied samples. While the micropore area decreases moderately (22.4%), the mesopore area decreases by ~96% (from 92.8 to 3.9 m^2/g), and the total pore volume is reduced by 92.9%. This pronounced loss of mesoporosity indicates extensive pore filling and/or blockage by CB[7]. The data suggest that CB[7] exhibits strong affinity toward the mesoporous channels, likely due to optimal molecular dimensions and favorable surface interactions, consistent with the pronounced FTIR carbonyl shift observed for this homolog.

The MBGs@CB[8] composite shows a 71.2% reduction in specific surface area (32.13 $m^2\ g^{-1}$), which is intermediate between CB[6] and CB[7]. The mesopore surface area decreases significantly (80.4%), whereas the micropore area is reduced by only 13.5%. Notably, the micropore volume remains nearly unchanged (3.3% decrease relative to pristine MBGs), while the total pore volume decreases by 69%. This behavior suggests that CB[8] preferentially interacts with mesopores without substantially affecting microporous domains, likely due to steric constraints associated with its larger cavity size.

3.5. Thermal Stability and Loading Analysis

To evaluate the loading content of cucurbit[n]urils within the MBG framework and to assess their thermal stability, TGA coupled with differential scanning calorimetry (DSC) was performed for all MBGs@CB[n] samples.

The TGA curve of MBGs@CB[6] shows a total mass loss of 32.7% over the investigated temperature range (Figure 4a). The remaining 67.3% residue corresponds primarily to the inorganic silicate matrix. The observed mass loss is attributed to thermal decomposition of the incorporated CB[6], confirming successful loading of the macrocycle. The relatively gradual decomposition profile and substantial residual mass indicate stable retention of CB[6] within the mesoporous structure. These results are consistent with FTIR observations suggesting interfacial interactions between CB[6] and surface silanol groups.

In contrast, MBGs@CB[7] exhibits a significantly higher mass loss of 54.7%, leaving a residual mass of 45.34%, as presented in Figure 4b. This pronounced weight reduction indicates a higher apparent organic content or a greater extent of thermally removable species. The sharper mass loss event observed in the DTG curve suggests that CB[7] is more readily decomposed or released upon heating. While BET analysis indicated

extensive pore occupation by CB[7], the thermal data suggest that its interaction with the silicate framework may involve a larger fraction of physically confined rather than strongly anchored molecules. This behavior correlates with the significant structural changes observed in the porosity analysis.

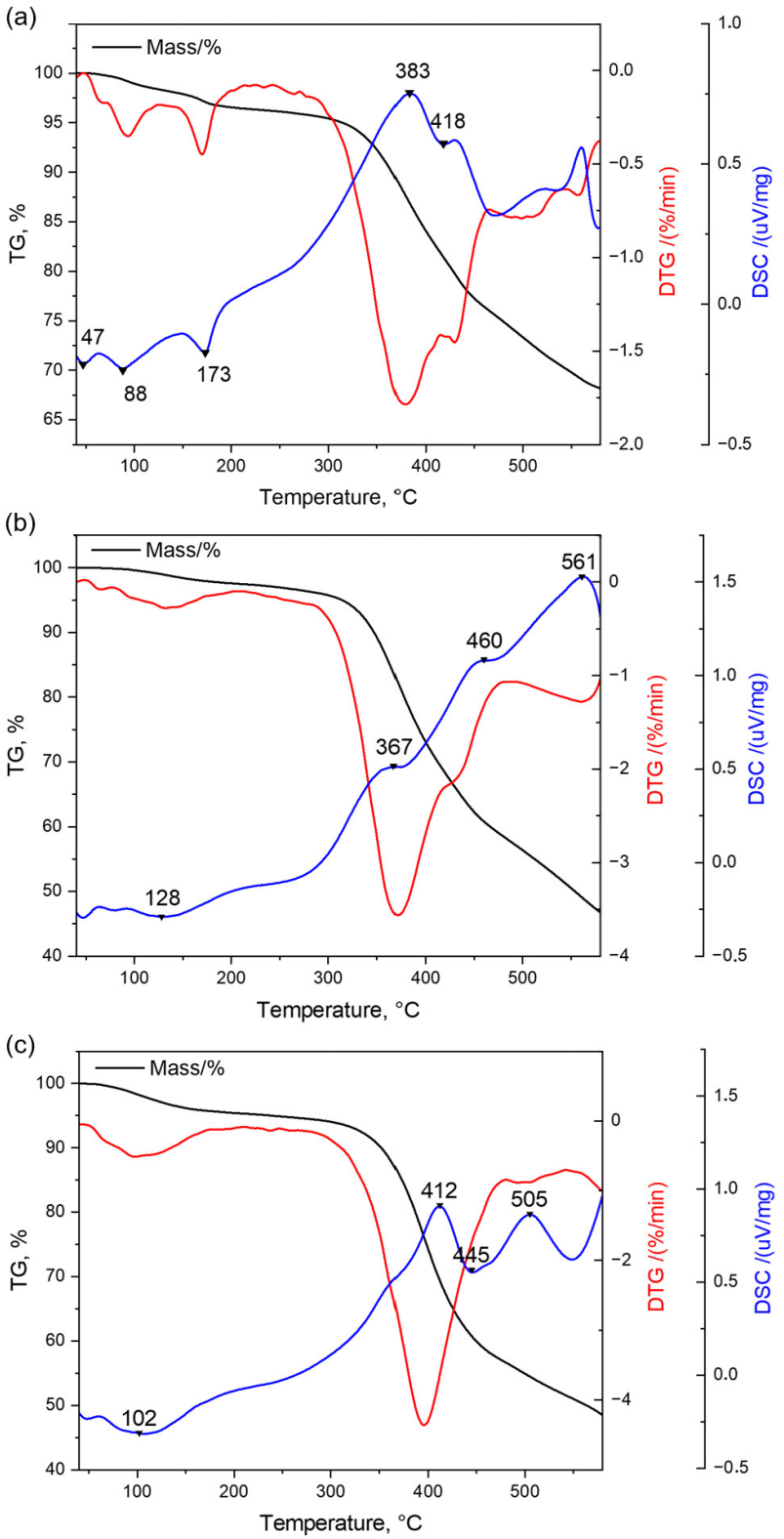


Figure 4. TGA and DSC curves of (**a**) MBGs@CB[6], (**b**) MBGs@CB[7], and (**c**) MBGs@CB[8] composites, illustrating the thermal decomposition behavior and relative loading of cucurbit[n]urils within the mesoporous bioactive glass framework.

Figure 4c displays a total mass loss of 53.9%, comparable to MBGs@CB[7] for the MBGs@CB[8] composite, with a residual mass of 46.14%. However, the DTG peak maximum is shifted toward higher temperatures (up to ~395 °C), indicating enhanced thermal stability relative to CB[7]. This shift suggests stronger or more stable confinement of CB[8] within the porous network. Combined with the BET results showing preserved microporosity, this behavior supports a model in which CB[8] is distributed both on the surface and within mesopores, achieving effective embedding without complete pore blockage.

The combined analysis of SEM, BET, FTIR, and TGA results reveals a size-dependent interaction pattern between cucurbit[n]urils and the MBG framework:

- CB[6]: Moderate loading with stable retention and partial pore occupation.
- CB[7]: Extensive mesopore filling with high apparent loading but lower thermal stability, suggesting a significant fraction of physically confined species.
- CB[8]: High loading with improved thermal stability and balanced preservation of pore structure.

These findings demonstrate that the interaction between CB[n] homologues and mesoporous bioactive glass is governed by macrocycle size and geometric compatibility with the pore architecture. Among the investigated systems, CB[8] appears to provide the most favorable compromise between loading efficiency, structural preservation, and thermal stability.

3.6. Molecular Modeling of CB[n]-SiO_2 Surface Interactions

To gain mechanistic insight into the experimentally observed size-dependent behavior, molecular mechanics calculations were performed to model the interaction of cucurbit[n]urils with a representative silica surface. An α-quartz SiO_2 unit cell was selected as a simplified surface model, and two orientations of CB[n] relative to the surface were considered: perpendicular (⊥) and parallel (∥) (Figure 5). While other tilted orientations are theoretically possible, they would yield interaction energies intermediate between the perpendicular and parallel extremes and would not affect the qualitative ranking of CB[n] surface affinity. Therefore, the two limiting cases (⊥ and ∥) are sufficient for the purpose of supporting the experimental trends. Computational simulations were performed under the assumptions detailed in Section 2.5.

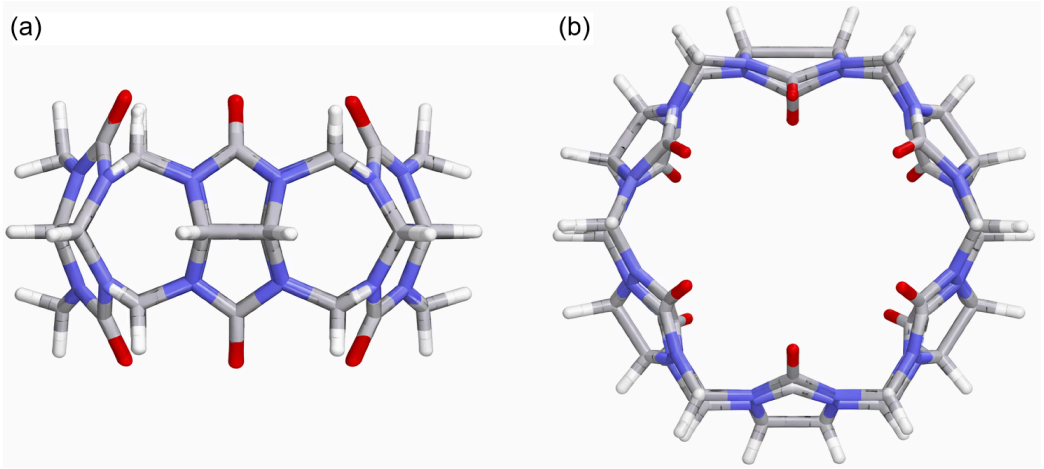


Figure 5. Schematic representation of the relative orientation of CB[n] molecules, (**a**) perpendicular (⊥) and (**b**) parallel (∥), considered for adsorption on the SiO_2 surface.

It should be noted that the calculations were performed under several simplifying assumptions, which limit their direct quantitative interpretation. The α-quartz model represents an idealized surface and does not fully capture the structural heterogeneity

of real MBG (e.g., defects, pore curvature, varying silanol density). The rigid surface approximation, gas-phase conditions, and single-molecule adsorption model neglect solvent effects, confinement effects, and intermolecular interactions between adjacent CB[n] molecules within the pores. Therefore, the calculated interaction energies should be considered as qualitative trends supporting the experimental observations rather than as quantitative predictions.

For CB[6], the most favorable interaction was observed in the perpendicular orientation, as shown in Figure 6a, with an interaction energy of -31.45 kcal mol^{-1} (Table 2). This orientation enables optimal alignment of the portal carbonyl groups toward surface silanol sites, promoting favorable electrostatic and hydrogen-bonding interactions compared to the parallel configuration (Figure 6b). The calculated interaction energy is consistent with the moderate pore occupation and stable thermal behavior observed experimentally.

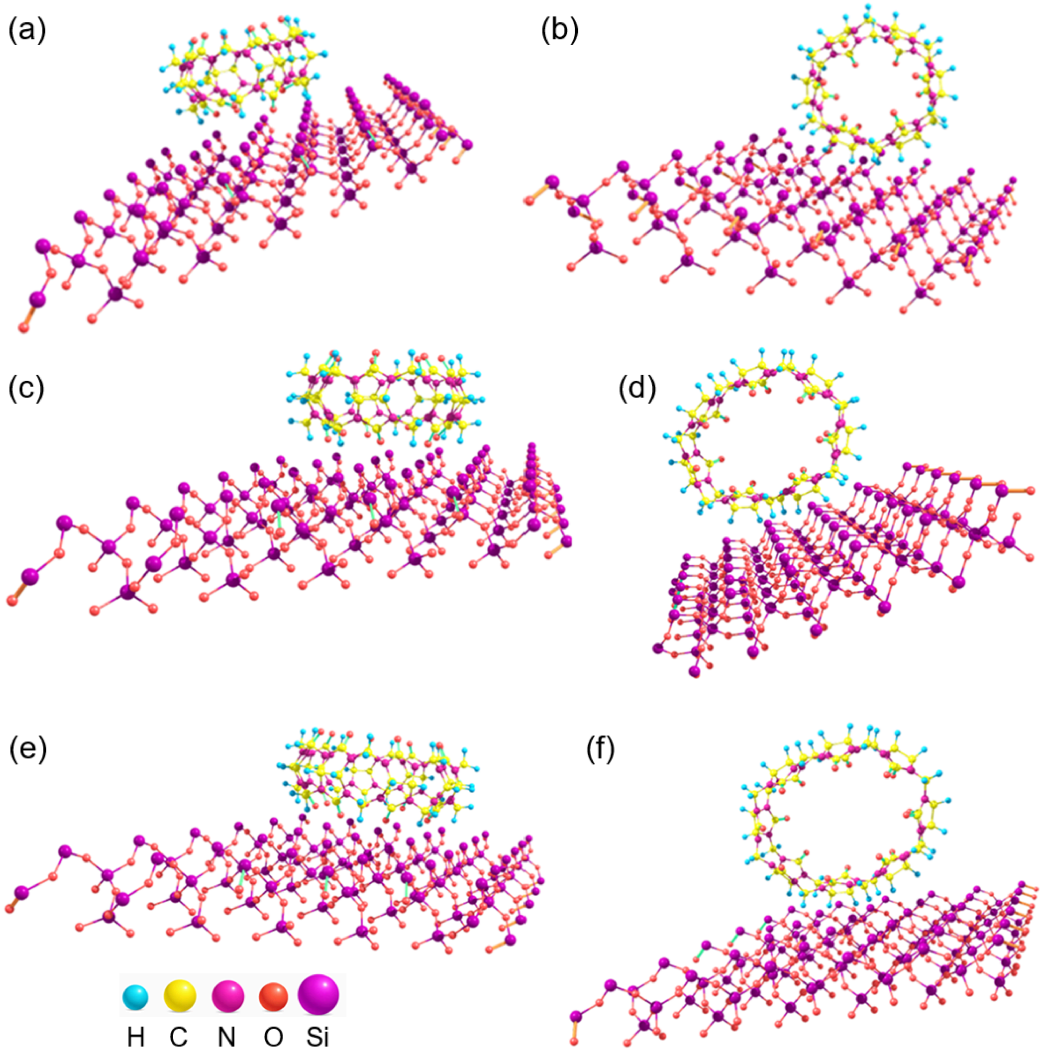


Figure 6. Optimized adsorption geometries obtained from molecular mechanics calculations for the interaction of cucurbit[n]urils with the α-quartz (SiO_2) surface: (**a**,**b**) CB[6], (**c**,**d**) CB[7], and (**e**,**f**) CB[8] in perpendicular (⊥) and parallel (||) adsorption orientations, respectively. Individual elements are represented by colored spheres (H, C, N, O, Si) for clarity.

Table 2. Calculated adsorption, deformation, and interaction energies (kcal·mol^{-1}) for CB[6], CB[7], and CB[8] on the α-quartz (SiO_2) surface in perpendicular (⊥) and parallel (||) orientations.

Sample	Energy, kcal mol^{-1}	Adsorption Orientations	
		Perpendicular (⊥)	Parallel (||)
CB[6]	$E_{adsorption}$	−27.80	−19.61
	$E_{deformation}$	3.65	0.77
	$E_{interaction}$	−31.45	−20.38
CB[7]	$E_{adsorption}$	−32.96	−19.85
	$E_{deformation}$	2.18	2.05
	$E_{interaction}$	−35.14	−21.91
CB[8]	$E_{adsorption}$	−34.14	−22.12
	$E_{deformation}$	0.41	0.58
	$E_{interaction}$	−34.5	−22.70

Among the investigated homologues, CB[7] exhibited the strongest calculated interaction energy in perpendicular orientation (−35.14 kcal mol^{-1}), as shown in Figure 6c. This result indicates a highly favorable electronic interaction between CB[7] and the silica surface at the molecular level. However, despite the high interaction energy, experimental data (TGA and BET) suggest partial instability or extensive pore blocking in the composite system. This apparent discrepancy may arise from steric constraints and packing effects within the mesoporous network, which are not fully captured in the isolated surface model. Thus, while CB[7] demonstrates strong intrinsic surface affinity, its larger effective footprint within confined pores may reduce practical stability under thermal treatment.

A similarly favorable interaction energy was calculated in the perpendicular orientation for CB[8], as shown in Figure 6e. Notably, the deformation (strain) energy of CB[8] upon adsorption was lower than that of CB[6] and CB[7], indicating reduced structural distortion during surface association. This suggests that CB[8] may achieve a more stable adsorption configuration, consistent with the observed DTG peak shift toward higher temperatures and the preservation of microporosity in BET analysis.

In line with prior simulation studies highlighting the role of composition in governing atomic-level flexibility in bioactive glasses [40], the present results further emphasize that molecular-scale interactions and geometric compatibility are key factors controlling interfacial stability and structural response in hybrid systems.

The computational results support the experimentally observed size-dependent interaction trend. While CB[7] exhibits the strongest intrinsic interaction energy, CB[8] appears to achieve a more favorable balance between adsorption energy and structural stability, due to lower deformation penalties and reduced steric strain within the porous framework. This balance may explain the improved thermal stability and partial preservation of porosity observed for MBGs@CB[8]. Overall, the modeling results reinforce the conclusion that macrocycle size and geometric compatibility play a critical role in governing the interfacial behavior of cucurbit[n]urils within mesoporous bioactive glass systems.

4. Conclusions

In this study, mesoporous bioactive glass composites functionalized with cucurbit[n]urils (CB[6], CB[7], and CB[8]) were successfully synthesized via aqueous deposition followed

by controlled solvent evaporation. FTIR spectroscopy confirmed the incorporation of macrocycles and revealed size-dependent carbonyl shifts, with the most pronounced perturbation observed for CB[7]. Nitrogen sorption analysis demonstrated that CB[6] caused moderate pore occupation (64% surface area reduction), CB[7] induced extensive mesopore blockage (92.4% reduction), while CB[8] preserved microporosity almost unchanged (only 3.3% decrease). TGA showed comparable loading for CB[7] and CB[8], yet MBGs@CB[8] exhibited enhanced thermal stability, with the DTG maximum shifted to ~395 °C. Molecular modeling supported these findings, indicating favorable adsorption geometry for all homologues. Collectively, CB[8] provides the most balanced combination of pore preservation, loading efficiency, and thermal stability, making it the most promising candidate for further functionalization in drug delivery and bone-regenerative applications.

Supplementary Materials: The following supporting information can be downloaded at: https://www.mdpi.com/article/10.3390/jcs10050255/s1, Figure S1. PXRD pattern of CB[6]; Figure S2. PXRD pattern of CB[7]; Figure S3. PXRD pattern of CB[8]; Figure S4. SEM images of the pristine MBGs sample.

Author Contributions: Conceptualization, G.Z., A.B. and R.Y.; methodology, G.Z., A.U., I.K. and R.R.; software, M.S. and A.K.; validation, A.U., S.M., M.S., A.K., R.R. and R.Y.; formal analysis, A.B.; investigation, G.Z., A.U. and I.K.; resources, S.M.; data curation, G.Z., A.U., S.M. and M.S.; writing—original draft preparation, G.Z.; writing—review and editing, G.Z., A.U., S.M., M.S., A.K., A.B., I.K., R.R. and R.Y.; visualization, S.M., M.S., A.K., I.K. and R.R.; supervision, A.B. and R.Y.; project administration, R.Y.; funding acquisition, A.B. All authors have read and agreed to the published manuscript.

Funding: This work was supported by Russian Science Foundation, grant RSF 24-43-20044 (to IK).

Data Availability Statement: The original contributions presented in this study are included in the article/Supplementary Material. Further inquiries can be directed to the corresponding author.

Acknowledgments: The authors express their gratitude to the L.N. Gumilyov Eurasian National University and National Research Tomsk State University for providing laboratory facilities and technical support during the research.

Conflicts of Interest: The authors declare no conflicts of interest.

References

1. Deanesly, R.; Parkes, A.S. Oestrogenic Action of Compounds of the Androsterone-Testosterone Series. *BMJ* **1936**, *1*, 257–258. [CrossRef] [PubMed]
2. Amato, S.F.; Ezzell, R.M. *Regulatory Affairs for Biomaterials and Medical Devices*; Elsevier: Amsterdam, The Netherlands, 2015.
3. Gorustovich, A.A.; Roether, J.A.; Boccaccini, A.R. Effect of Bioactive Glasses on Angiogenesis: A Review of In Vitro and In Vivo Evidences. *Tissue Eng. Part B Rev.* **2010**, *16*, 199–207. [CrossRef] [PubMed]
4. Hench, L.L.; Hench, J.W.; Greenspan, D. Bioglass: A short history and bibliography. *J. Aust. Ceram. Soc.* **2004**, *40*, 1–42.
5. Nandi, S.K.; Mahato, A.; Kundu, B.; Mukherjee, P. Doped Bioactive Glass Materials in Bone Regeneration. In *Advanced Techniques in Bone Regeneration*; Zorzi, A.R., de Miranda, J.B., Eds.; IntechOpen: London, UK, 2016; pp. 275–328.
6. Hench, L.L. The story of Bioglass®. *J. Mater. Sci. Mater. Med.* **2006**, *17*, 967–978. [CrossRef]
7. Hench, L.L. Bioceramics. *J. Am. Ceram. Soc.* **1998**, *81*, 1705–1728. [CrossRef]
8. Vallet-Regí, M.; Ragel, C.V.; Salinas, A.J. Glasses with Medical Applications. *Eur. J. Inorg. Chem.* **2003**, *2003*, 1029–1042. [CrossRef]
9. Li, R.; Clark, A.E.; Hench, L.L. An investigation of bioactive glass powders by sol-gel processing. *J. Appl. Biomater.* **1991**, *2*, 231–239. [CrossRef]
10. Ylänen, H.O. Clinical application of bioactive glasses. In *Bioceramics and Their Clinical Applications*; Kokubo, T., Ed.; Woodhead Publishing: Cambridge, UK, 2008; pp. 571–582.
11. Jones, J.R. Review of bioactive glass: From Hench to hybrids. *Acta Biomater.* **2013**, *9*, 4457–4486. [CrossRef]
12. Vallet-Regí, M.; González-Calbet, J.M. Calcium phosphates as substitution of bone tissues. *Prog. Solid State Chem.* **2004**, *32*, 1–31. [CrossRef]

13. Rondinella, A.; Marin, E.; McEntire, B.; Bock, R.; Bal, B.S.; Zhu, W.L.; Yamamoto, K.; Pezzotti, G. Bioceramics are Not Bioinert: The Role of Oxide and Non-Oxide Bioceramics on the Oxidation of UHMWPE Components in Artificial Joints. *Key Eng. Mater.* **2018**, *782*, 165–175. [CrossRef]
14. Best, S.M.; Porter, A.E.; Thian, E.S.; Huang, J. Bioceramics: Past, present and for the future. *J. Eur. Ceram. Soc.* **2008**, *28*, 1319–1327. [CrossRef]
15. Lin, K.; Wu, C.; Chang, J. Advances in synthesis of calcium phosphate crystals with controlled size and shape. *Acta Biomater.* **2014**, *10*, 4071–4102. [CrossRef] [PubMed]
16. Vallet-Regí, M.; Ruiz-Hernández, E. Bioceramics: From Bone Regeneration to Cancer Nanomedicine. *Adv. Mater.* **2011**, *23*, 5177–5218. [CrossRef] [PubMed]
17. Marchenko, E.; Luchsheva, V.; Baigonakova, G.; Bakibaev, A.; Vorozhtsov, A. Functionalization of the Surface of Porous Nickel–Titanium Alloy with Macrocyclic Compounds. *Materials* **2022**, *16*, 66. [CrossRef]
18. Kolesnichenko, I.V.; Anslyn, E.V. Practical applications of supramolecular chemistry. *Chem. Soc. Rev.* **2017**, *46*, 2385–2390. [CrossRef] [PubMed]
19. Arcos, D.; Portolés, M.T. Mesoporous Bioactive Nanoparticles for Bone Tissue Applications. *Int. J. Mol. Sci.* **2023**, *24*, 3249. [CrossRef]
20. Vulpoi, A.; Botiz, I. Mesoporous Bioactive Glasses: A Review on Structure-Directing-Based Synthesis, Characterization, and Biomedical Applications. *Materials* **2026**, *19*, 876. [CrossRef]
21. Langer, R. Drug delivery. Drugs on target. *Science* **2001**, *293*, 58–59. [CrossRef]
22. Deanesly, R.; Parkes, A.S. Testosterone. *Br. Med. J.* **1936**, *1*, 527–528. [CrossRef]
23. Hench, L.L.; Jones, J.R. Bioactive Glasses: Frontiers and Challenges. *Front. Bioeng. Biotechnol.* **2015**, *3*, 194. [CrossRef]
24. Buser, D.; Weber, H.; Lang, N.P. Tissue integration of non-submerged implants. l-year results of a prospective study with 100 ITI hollow-cylinder and hollow-screw implants. *Clin. Oral Implant. Res.* **1990**, *1*, 33–40. [CrossRef]
25. El-Rashidy, A.A.; Roether, J.A.; Harhaus, L.; Kneser, U.; Boccaccini, A.R. Regenerating bone with bioactive glass scaffolds: A review of in vivo studies in bone defect models. *Acta Biomater.* **2017**, *62*, 1–28. [CrossRef]
26. Alešković, M.; Šekutor, M. Overcoming barriers with non-covalent interactions: Supramolecular recognition of adamantyl cucurbit[*n*]uril assemblies for medical applications. *RSC Med. Chem.* **2023**, *15*, 433–471. [CrossRef]
27. Burkhanbayeva, T.; Ukhov, A.; Assylbekova, D.; Mussina, Z.; Kurzina, I.; Abilkasova, S.; Bakibaev, A.; Issabayeva, M.; Yerkassov, R.; Shaikhova, Z. The Role of Methods for Applying Cucurbit[6]uril to Hydroxyapatite for the Morphological Tuning of Its Surface in the Process of Obtaining Composite Materials. *Materials* **2024**, *17*, 4995. [CrossRef]
28. Burkhanbayeva, T.; Ukhov, A.; Fedorishin, D.; Gubankov, A.; Kurzina, I.; Bakibaev, A.; Yerkassov, R.; Mashan, T.; Suyundikova, F.; Nurmukhanbetova, N.; et al. Development of New Composite Materials by Modifying the Surface of Porous Hydroxyapatite Using Cucurbit[n]urils. *Materials* **2024**, *17*, 2041. [CrossRef]
29. Xie, X.; Li, X.; Luo, H.; Lu, H.; Chen, F.; Li, W. The Adsorption of Reactive Blue 19 Dye onto Cucurbit[8]uril and Cucurbit[6]uril: An Experimental and Theoretical Study. *J. Phys. Chem. B* **2016**, *120*, 4131–4142. [CrossRef]
30. Li, X.; Xie, X.; Luo, H.; Li, L.; Li, Z.; Xue, Z.; Li, W. Adsorption of reactive yellow X-RG and reactive brilliant red X-3B onto cucurbit[8]uril and cucurbit[6]uril: Effect factors, adsorption behavior and mechanism study. *J. Colloid Interface Sci.* **2017**, *498*, 31–46. [CrossRef]
31. Luo, H.; Huang, X.; Luo, Y.; Li, Z.; Li, L.; Gao, C.; Xiong, J.; Li, W. Adsorption behavior and mechanism of acidic blue 25 dye onto cucurbit[8]uril: A spectral and DFT study. *Spectrochim. Acta Part A Mol. Biomol. Spectrosc.* **2018**, *193*, 125–132. [CrossRef]
32. Corda, E.; Hernandez, M.; Sanchez-Cortes, S.; Sevilla, P. Cucurbit[n]urils (n = 6–8) used as host molecules on supramolecular complexes formed with two different drugs: Emodin and indomethacin. *Colloids Surf. A Physicochem. Eng. Asp.* **2018**, *227*, 66–75. [CrossRef]
33. Wu, X.; Zhang, Y.-M.; Liu, Y. Nanosupramolecular assembly of amphiphilic guest mediated by cucurbituril for doxorubicin delivery. *RSC Adv.* **2016**, *6*, 99729–99734. [CrossRef]
34. Yu, G.; Chen, X. Host-Guest Chemistry in Supramolecular Theranostics. *Theranostics* **2019**, *9*, 3041–3074. [CrossRef]
35. Wheate, N.J.; Buck, D.P.; Day, A.I.; Collins, J.G. Cucurbit[n]uril binding of platinum anticancer complexes. *Dalton Trans.* **2005**, *3*, 451–458. [CrossRef]
36. Colaco, V.; Jadhav, S.R.; Bandi, S.P.; Datta, D.; Dhas, N.; Thakur, G.; Ramesh, B.V.; Alizadeh, B. Multifunctional Application of Supramolecular Cucurbiturils as Encapsulating Hosts in Drug Delivery: A Review. *Int. J. Pharm.* **2025**, *681*, 125801. [CrossRef]
37. Fedorishin, D.A.; Mousanezhad, S.; Shapovalova, Y.G.; Kurzina, I.A.; Bakibaev, A.A. Biocompatibility of Cucurbit[n]urils. *Chim. Techno Acta* **2026**, *13*, 9216. [CrossRef]
38. Ukhov, A.E.; Larikov, V.A.; Baigonakova, G.A.; Marchenko, E.S.; Gubonkov, A.; Bakibaev, A. Preparation of New Composite Materials Based on Urea-Containing Macrocyclic Compounds and Porous Titanium Nickelide. *Vestn. Tomsk. Gos. Univ. Khimiya* **2024**, *36*, 152–168. [CrossRef]

39. Kim, J.; Jung, I.-S.; Kim, S.-Y.; Lee, E.; Kang, J.-K.; Sakamoto, S.; Yamaguchi, K.; Kim, K. New Cucurbituril Homologues: Syntheses, Isolation, Characterization, and X-ray Crystal Structures of Cucurbit[*n*]uril (*n* = 5, 7, and 8). *J. Am. Chem. Soc.* **2000**, *122*, 540–541. [CrossRef]
40. Tian, K.V.; Chass, G.A.; Di Tommaso, D. Simulations Reveal the Role of Composition into the Atomic-Level Flexibility of Bioactive Glass Cements. *Phys. Chem. Chem. Phys.* **2016**, *18*, 837–845. [CrossRef]

Disclaimer/Publisher's Note: The statements, opinions and data contained in all publications are solely those of the individual author(s) and contributor(s) and not of MDPI and/or the editor(s). MDPI and/or the editor(s) disclaim responsibility for any injury to people or property resulting from any ideas, methods, instructions or products referred to in the content.